Remediation of liquefaction effects for an embankment using soil-cement walls: Centrifuge and numerical modeling

Ross W Boulanger, Mohammad Khosravi, Ali Khosravi, & Daniel W. Wilson
Department of Civil and Environmental Engineering, University of California, Davis, CA, USA

ABSTRACT
Numerical simulations of a centrifuge model test of an embankment on a liquefiable foundation layer treated with soil-cement walls are presented. The centrifuge model was tested on a 9-m radius centrifuge and corresponded to a 28 m tall embankment underlain by a 9 m thick saturated loose sand layer. Soil-cement walls were constructed through the loose sand layer over a 30 m long section near the toe of the embankment and covered with a 7.5 m tall berm. The model was shaken with a scaled earthquake motion having peak horizontal base accelerations of 0.05 g, 0.26 g, 0.54 g in the first, second, and third events, respectively. The latter two shaking events caused liquefaction in the loose sand layer. The soil-cement walls sheared through their full length in the last shaking event. The results of the centrifuge model test and two-dimensional nonlinear dynamic simulations are compared. Capabilities and limitations in the two-dimensional simulations of soil-cement wall reinforcement systems, with both liquefaction and soil-cement cracking effects, are discussed. Implications for practice are discussed.

1 INTRODUCTION

Soil-cement grid and wall systems have been used to remediate embankment dams and other civil infrastructure against the effects of earthquake-induced liquefaction in their foundations. Soil-cement treatments have the advantage that they can be constructed in a wide range of soils, including silty soils that can be difficult to treat by densification techniques. A soil-cement grid or wall system is often constructed near the toe of an embankment and covered with an overlying berm to increase confinement and reduce deformation modes that bypass the treatment zone. An example of this type of configuration is the remediation at the 24-m tall Clemson Upper and Lower Diversion Dams (Wooten and Foreman 2005) as shown in Figure 1. Other embankment dam remediation projects using soil-cement grid or wall systems in the US include: Sunset North Basin Dam, CA (about 23 m high; Barron et al. 2006); San Pablo Dam, CA (about 44 m high; Kirby et al. 2010); Perris Dam, CA (about 39 m high; Friesen and Balakrishnan 2012), and Chabot Dam, CA (about 30 m high; EBMUD).

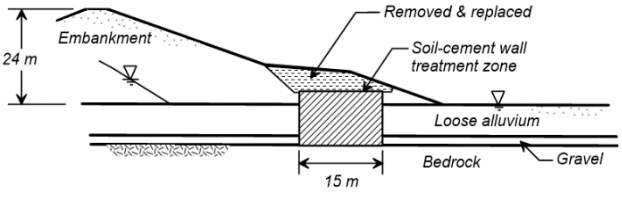

Figure 1. Soil-cement shear walls at Clemson Diversion Dams, SC (after Wooten and Foreman 2005)

The seismic performance of soil-cement grids and walls have been studied using three-dimensional (3D) analysis methods (e.g., Fukutake and Ohtsuki 1995, Namikawa et al. 2007), but design practices generally rely on two-dimensional (2D) approximations with equivalent composite strengths for the treatment zones (e.g. Wooten and Foreman 2005, Barron et al. 2006, Kirby et al. 2010, Friesen and Balakrishnan 2012). Some common concerns the design of soil-cement grids for liquefaction remediation include the potential for cracking and brittle failure in the soil-cement elements, the ability of 2D analysis procedures to approximate the 3D response, and the lack of experimental or case history data to validate 2D or 3D numerical analysis methods.

This paper presents results of centrifuge model tests and numerical simulations of an embankment on a liquefiable foundation layer treated with soil-cement walls. The centrifuge model was tested on a 9-m radius centrifuge and corresponded to a 28 m tall embankment underlain by a 9 m thick saturated loose sand layer (prototype units). Soil-cement grids were positioned through the loose sand layer near the toe of the embankment and covered with a berm. The model was shaken three times with a scaled earthquake motion; the peak horizontal base accelerations (PBA) were 0.05 g, 0.26 g and 0.54 g, respectively. The latter two events liquefied the loose sand layer. The soil-cement walls developed limited cracking in the 0.26 g shaking event and sheared through their full length in the 0.54 g event. Two-dimensional nonlinear dynamic analyses were performed using the finite difference program FLAC (Itasca 2011) and the user-defined constitutive model PM4Sand (Boulanger and Ziotopoulou 2015) for the sands. The treatment zone was represented with area-averaged composite properties as is common in design practice. The centrifuge model test and numerical simulation procedures are described, followed by

comparisons of the measured and simulated responses. Implications of the results for practice are discussed.

2 CENTRIFUGE MODEL TEST

The centrifuge model was tested in a flexible shear beam container at a centrifugal acceleration of 65 g on the UC Davis 9-m radius centrifuge. Standard scaling laws are followed and results are presented in prototype units unless otherwise specified. The experiment and data are documented for distribution in Khosravi et al. (2016) and summarized in Khosravi et al. (2017).

The centrifuge model configuration (Figure 2) consisted of a foundation layer of loose Ottawa F-65 sand (relative density, D_r = 42%; D_{10} = 13 mm), an embankment and berm of dry, dense Monterey #0/30 sand (D_r = 85%; D_{10} = 0.4 mm), and a set of parallel soil-cement panels over a 30-m long section near the toe of the embankment. The pore fluid was a methylcellulose solution with a viscosity about 15 times that of water. The water table was above the top of the foundation layer and slightly above the tops of the walls. A thin layer of Monterey medium aquarium sand (D_{10} = 1.7 mm) was placed at the water surface elevation to provide a capillary break during model construction.

The soil-cement walls were formed and cured in molds and then arranged in the model container prior to pluviation of the foundation sand layer. The walls were 1.4 m thick and spaced 5.8 m apart (center to center), for an area replacement ratio of A_r = 24%. The soil-cement had an average unconfined compressive strength (q_{ucs}) of 2.06 MPa at the time of centrifuge testing. The walls were set into preformed slots in a concrete base layer and grouted into position.

Seventeen crack detectors were embedded in four of the soil-cement walls at the time they were formed. The crack detectors were 2-mm diameter pencil leads connected to a circuit by wires at each end (Tamura et al. 2017). These brittle conductors provide a binary indication of if, and when, cracking occurs. The pencil leads were oriented vertically at different locations along the walls, with their lower end below the top of the concrete base.

The model was also extensively instrumented with accelerometers, pore pressure transducers, and displacement transducers as described in Khosravi et al. (2017). The locations of the transducers whose recordings are later compared with simulation results are shown on the cross-sections in Figure 3. A photograph of the model prior to testing is shown in Figure 4; the embankment crest is on the left side of the photo, and the blue sand marker lines are used to track surface deformations between shaking events.

The model was shaken three times with a scaled version of a recording from Port Island in the 1995 Kobe earthquake. The first shaking event had a PBA = 0.05 g, for which the response was essentially elastic with no excess pore pressure generated. The second shaking event had a PBA = 0.26 g, which triggered liquefaction in the saturated sand layer but caused only minor cracking in the soil-cement walls. The third shaking event was applied long after full dissipation of the excess pore pressures from the second event; it had a PBA = 0.54 g, triggered liquefaction throughout the saturated sand layer, and caused the soil-cement walls to develop shears/cracks through their full lengths. The crest settled about 0.7 m and the toe berm displaced laterally about 1.3 m in the PBA = 0.54 g event, whereas movements in the PBA = 0.26 g event were only a quarter to half these amounts.

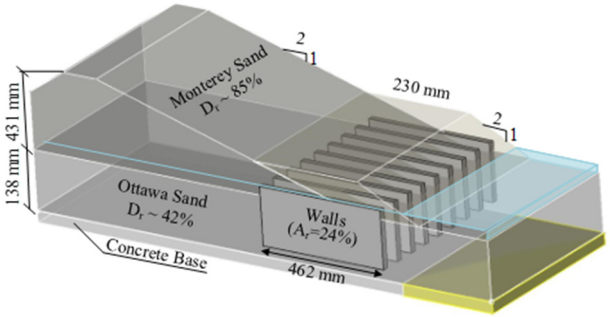

Figure 2. Centrifuge model configuration with dimensions in model scale

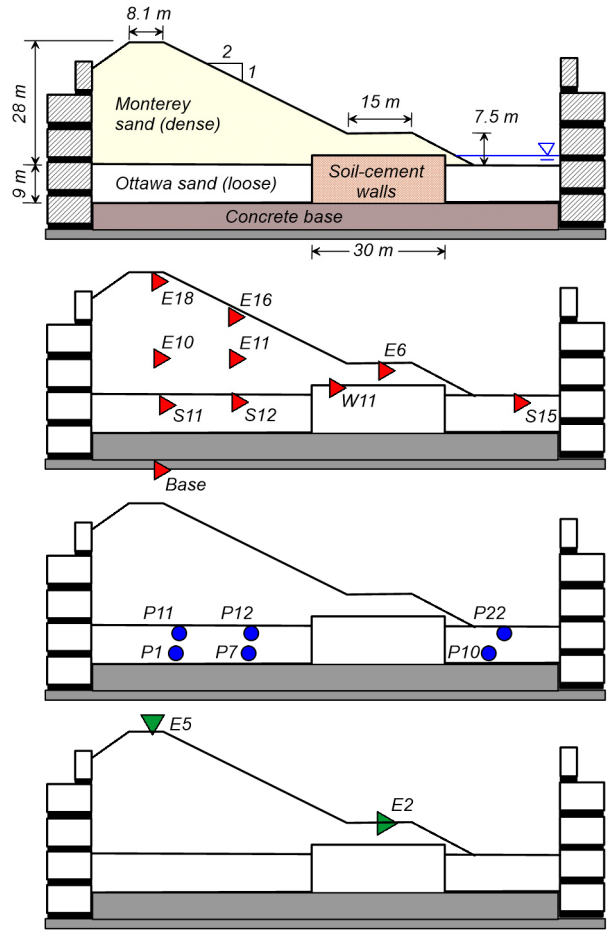

Figure 3. Cross-sections showing model dimensions (prototype scale) and the locations of accelerometers (red triangles), pore pressure transducers (blue circles), and displacement transducers (green triangles) that are later compared with simulation results

A photograph of the soil-cement walls when the foundation soils had been excavated to the elevation of a blue paper marker is shown in Figure 5. The blue markers were placed flush against the faces of the soil-cement walls on the upstream and downstream faces during construction. The blue markers have been pushed forward between the soil-cement walls on the upstream side, and pushed away from the walls by up to 0.8 m on the downstream side. These photos illustrate how the loose sand between the walls, which liquefied during strong shaking, appears to have displaced downslope relative to the walls during the course of imposed shaking.

A photograph of the soil-cement walls during model dissection after testing is shown in Figure 6. Crack detectors indicate that only portions of the panels were cracked during the PBA = 0.26 g event, such that the majority of damage and the offsets along the cracks occurred during the larger PBA = 0.54 g shaking event.

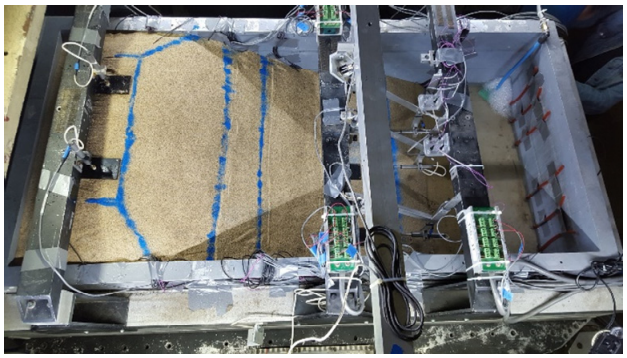

Figure 4. Photograph of model mounted on the centrifuge; lines of blue sand are for visual reference

Figure 5. Post-test excavation photos of the soil-cement panels (toe of berm is to left side of photos)

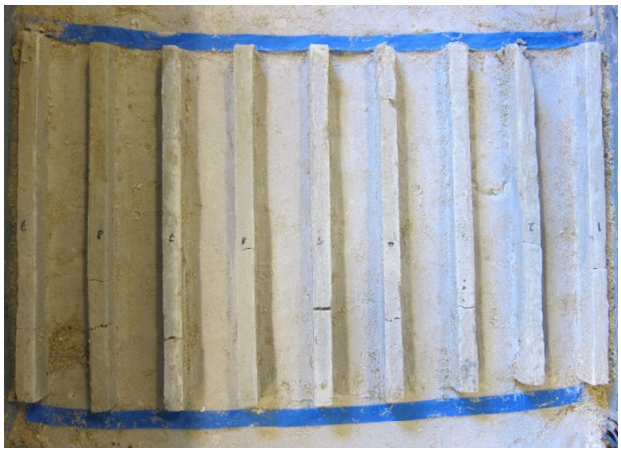

Figure 6. Post-test excavation with exposed paper markers (originally aligned in contact with panels) showing the liquefied sand moved more than the soil-cement panels (toe of berm is to bottom of photo)

3 NUMERICAL SIMULATION MODEL

Two-dimensional (2D) nonlinear dynamic analyses were performed using the finite difference program FLAC (Itasca 2016). The mesh and material zones are shown in Figure 7. Analyses were performed in large-strain mode with coupled pore water flow. Analyses used 0.5% Rayleigh damping at a frequency of 1 Hz.

The sands were modeled using the user-defined constitutive model PM4Sand version 3, which is a stress-ratio controlled, critical state compatible, bounding surface plasticity model developed for earthquake engineering applications (Boulanger and Ziotopoulou 2015, Ziotopoulou and Boulanger 2016). This constitutive model requires specification of three primary input parameters; apparent relative density D_r, shear modulus coefficient G_o, and contraction rate parameter h_{po}. The optional secondary parameters receive default values per the calibration described by Ziotopoulou and Boulanger (2013) if the user does not specify them. The dynamic link library and example files for this model for use with FLAC is available for download at https://pm4sand.engr.ucdavis.edu/.

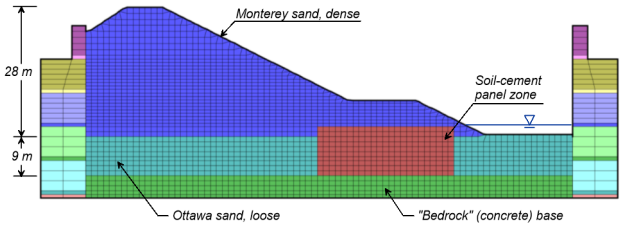

Figure 7. Two-dimensional mesh and material zones

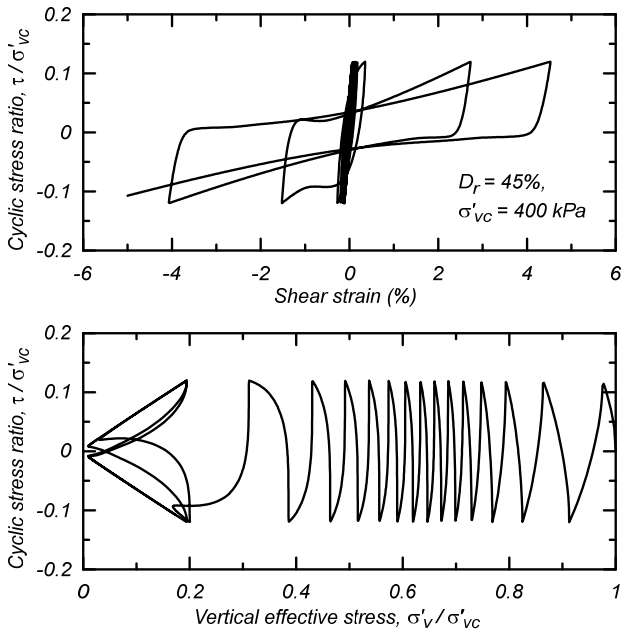

Figure 8. Response of calibrated PM4Sand model in cyclic undrained simple shear loading with zero initial static shear stress

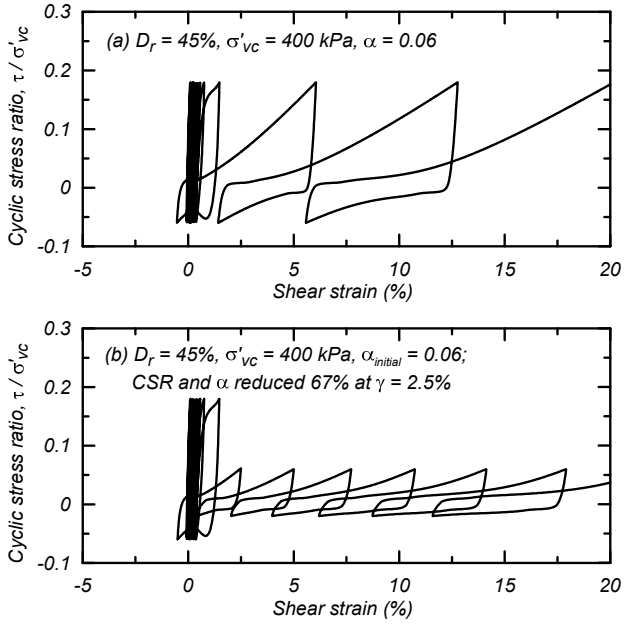

Figure 9. Response of calibrated PM4Sand model in cyclic undrained simple shear loading with an initial static shear stress ratio of α = 0.06: (a) with a uniform applied CSR, and (b) with the CSR and α reduced 67% once the peak shear strain reached 2.5%

The parameters for the loose sand layer were obtained by calibration against results of cyclic direct simple shear tests on Ottawa F-65 sand by Parra Bastidas et al. (2016). The cyclic stress ratio (CSR) to cause a peak shear strain of 3% (or an excess pore pressure ratio of 100%) in 15 uniform loading cycles at a vertical effective consolidation stress of 400 kPa was 0.093 for virgin specimens (i.e. applicable for the PBA = 0.05 g and 0.26 g shaking events) and 0.120 after one liquefaction event (i.e. applicable for the PBA = 0.54 g shaking event). The post-liquefaction reconsolidation after the first event caused a small increase in cyclic strength and density (estimated D_r = 45% versus 42%). The calibrated parameters for these analyses are D_r = 42%, G_o = 770, and h_{po} = 0.54 for the PBA = 0.26 g event, and D_r = 45%, G_o = 788, and h_{po} = 1.20 for the PBA = 0.54 g event. In addition, two secondary parameters were assigned values based on the available index test data for Ottawa F-65 sand: maximum void ratio e_{max} = 0.83 and minimum void ratio e_{min} = 0.51. The response of the constitutive model with the calibration for the second event is illustrated in Figure 8 showing the stress-strain and stress path responses to undrained, uniform cyclic, direct simple shear loading with an initial static shear stress ratio ($\alpha = \tau_{hv}/\sigma'_{vo}$) of zero.

The undrained cyclic loading response of the calibrated model with a nonzero static shear stress bias is important for these analyses of sloping ground conditions. The response of PM4Sand under sloping ground conditions with irregular cyclic loading is described in Ziotopoulou and Boulanger (2016), and illustrated by two examples in Figure 9. The response in Figure 9a shows the stress-strain response for the same loading conditions as previously shown in Figure 8, except with α = 0.06 instead of zero. The presence of the static shear stress bias causes shear strains to accumulate rapidly in the direction of the shear stress bias, as expected. The response in Figure 9b shows the same loading again, except that the CSR and α are both reduced by 67% once the shear strain has exceeded 2.5%. This example illustrates how a drop in imposed loading during seismic loading slows the rate of shear strain accumulation. These single-element loading responses can later be qualitatively compared to the stress-strain responses obtained for points within the system model, as one additional basis for evaluating the consistency of the material and system responses.

The parameters for the dense coarse Monterey sand were similar to those used by Armstrong and Boulanger (2015). The three primary parameters were D_r = 85%, G_o = 1427, and h_{po} = 1.9. The secondary parameters assigned non-default values were e_{max} = 0.84, e_{min} = 0.54, and n_b = 0.6. The bounding surface parameter n_b was increased from 0.5 (default value) to 0.6 to increase peak effective friction angles by a couple degrees, thereby being in better agreement with peak friction angles predicted for this dense sand by Bolton's (1986) relationship.

The soil-cement treatment zone was modeled using a Mohr Coulomb (c-ϕ) model with area-weighted cohesion and friction angle properties. The soil-cement's average undrained shear strength during strong shaking was taken as 80% of the peak undrained shear strength, or $(S_u)_{wall}$ = $0.8(q_{ucs}/2)$ = 0.82 MPa, to allow for some strain softening as the walls deform. This average resistance is intended to account for the actual shear resistance being closer to peak strength early in shaking and more than 20% below peak strength late in shaking. The saturated loose sand layer was assumed to contribute zero shear resistance to the composite system because its stress-strain response

would be much softer than that of the soil-cement walls after it liquefies. Thus, the equivalent composite shear strength for the treatment zone in the loose sand layer was taken as $c = A_r \cdot (S_u)_{wall} = 0.198$ MPa with $\phi = 0$ for the 2D numerical analyses. The dense Monterey sand is assumed to contribute shear resistance to the composite system because it is not expected to liquefy during shaking. Thus, the equivalent composite shear strength for the treatment zone in the dense Monterey sand was taken as $c = 0.198$ MPa with $\phi = 32$ degrees. The elastic modulus of the soil-cement (E_{sc}) was taken as 300 q_{ucs}. The equivalent composite elastic and bulk moduli of the treatment zone were taken as $A_r \cdot E_{sc}$ and $1.33 \cdot A_r \cdot E_{sc}$, respectively.

The flexible shear beam container and the concrete base inside the container were modeled using linear elastic materials. The mass and lateral stiffness of the container elements in the 2D model were computed as the actual mass and lateral stiffness of the 3D model container divided by the width of the enclosed soil mass (i.e. proportioning mass and stiff per unit width of soil).

Hydraulic conductivities (k) were assumed isotropic for both soils and the treatment zone. The loose Ottawa sand layer was assigned k = 0.0192 cm/s based on laboratory tests data summarized in Parra Bastidas et al. (2016). The dense Monterey sand was assigned a k ten times that of the Ottawa sand where it was saturated and one tenth that of the Ottawa sand where it was unsaturated. The effect of partial saturation on k was estimated using published data and generalized relationships (e.g. Zhang and Fredlund 2015). The soil-cement treatment zone was assigned area-weighted values of hydraulic conductivity.

4 INITIAL STATIC STRESS CONDITIONS

The initial static stress conditions for the numerical model were established using gravity turn-on with the simpler Mohr-Coulomb model used for all materials. The shear moduli for all sand materials were taken as confinement dependent, with the shear moduli computed based on estimated values for mean effective stress at each depth. This approach does not reproduce the complex loading history associated with centrifuge model construction at 1 g followed by spin-up, but the explicit modeling of those steps would not necessarily produce improved results. Instead, the intent is to produce initial static stress conditions that are reasonable and consistent with expected patterns. After the initial stresses are initialized, the constitutive models for the sand are switched to PM4Sand, equilibrium is solved for again, and the model is ready for dynamic loading.

The initial static stress conditions prior to dynamic loading are described in Figure 10 in terms of the vertical effective stress (σ'_{vo}), the coefficient of lateral earth pressure (K_o), and the initial static shear stress ratio on horizontal planes (α). The contours of σ'_{vo} are smooth and approximately parallel to the ground surface. The values of K_o are between 0.4 and 0.5 throughout most of the embankment and foundation, with higher values near the face of the embankment or downslope face of the berm. The values of $\alpha = \tau_{vh}/\sigma'_{vo}$ are between 0.0 and 0.3 for most of the body of the embankment and foundation, with higher values near the face of the embankment and berm slopes. The greater height of soil against the left side of the container causes the container to deform leftward; this causes an increase in the lateral stresses (both normal and shear) in the foundation soil against the right side of the container, and it causes small variations in stress conditions near each rubber ring on the left side of the container.

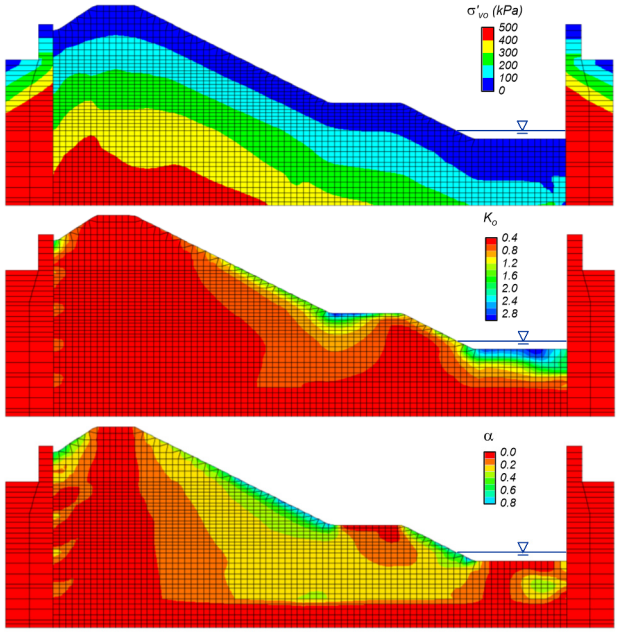

Figure 10. Initial static stress conditions: vertical effective stress, coefficient of lateral earth pressure at rest, and initial static shear stress ratio on horizontal planes.

5 DYNAMIC SIMULATION RESULTS

Numerical simulations were compared to measured responses for the PBA = 0.26 g and 0.54 g shaking events in terms of the accelerations, pore pressures, displacements, deformation patterns, and soil-cement damage patterns. Results for the PBA = 0.54 g event using the baseline set of input parameters, as described above, are presented to illustrate these comparisons.

5.1 Kobe event with PBA = 0.26 g

Simulated and measured accelerations for the PBA = 0.26 g event are compared in Figure 11 for several points in the embankment, toe berm, foundation layer, and base (locations shown in Figure 3). The simulated acceleration time series are in reasonable agreement with the recorded accelerations throughout the embankment and foundation.

Simulated and measured pore pressures for several points in the loose sand layer (locations shown in Figure 3) are compared in Figure 12. The measured excess pore pressures are far greater under the embankment (left two columns in Figure 12) than in the free field beyond the toe (right column in Figure 12), reflecting the differences in

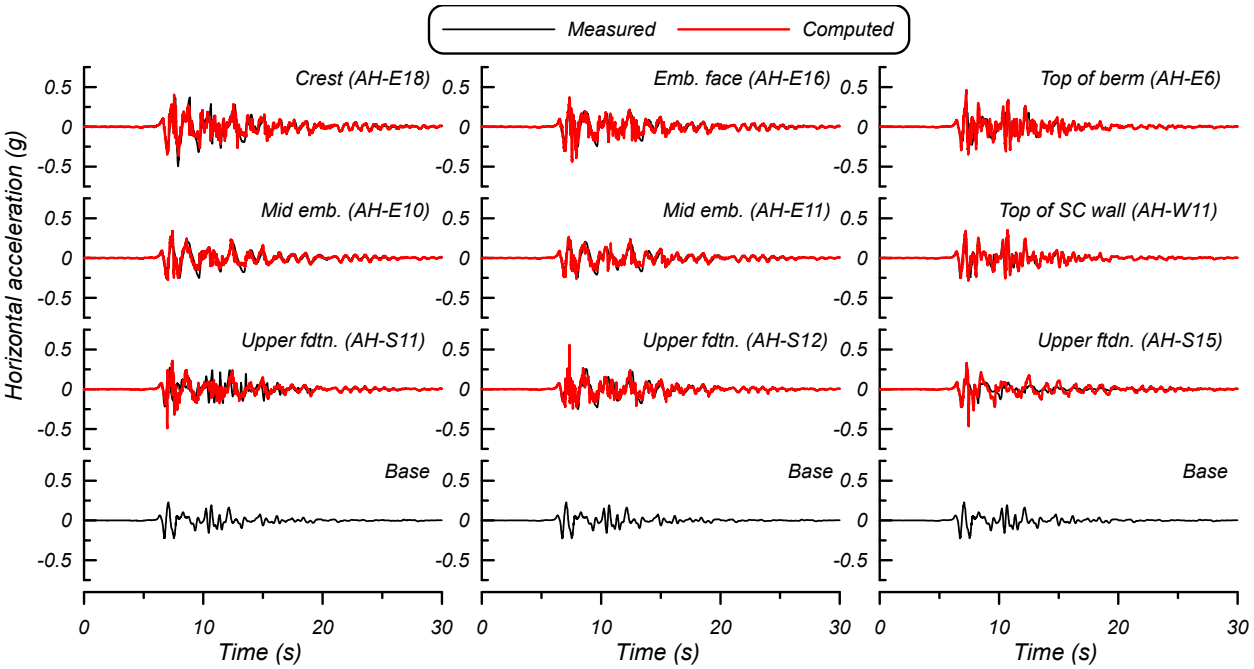

Figure 11. Measured and computed accelerations for the Kobe 0.26 g event

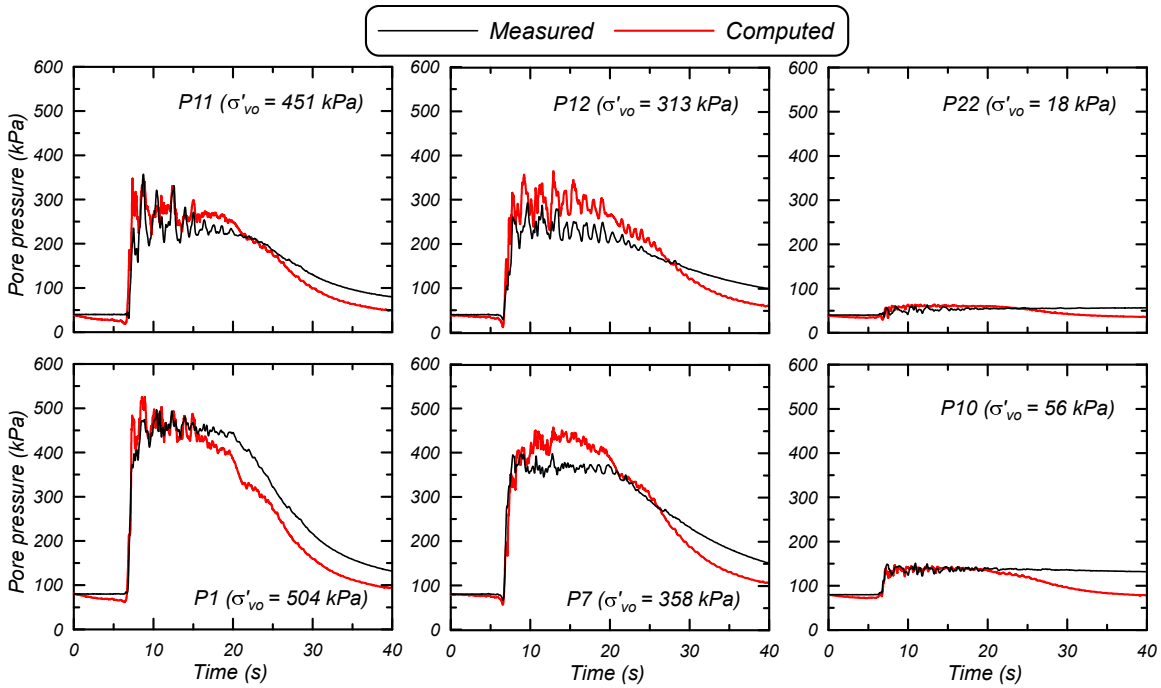

Figure 12. Measured and computed excess pore water pressures for the Kobe 0.26 g event

overburden stresses at these points. The pore pressures rise to values equal to the estimated overburden stresses at these points, indicating that excess pore pressure ratios of, or near, 100% were triggered throughout the loose sand layer. The simulations reasonably track the rise in excess pore pressures, their peak values, and their dissipation rates after the end of strong shaking.

Simulated and measured displacements for the crest and berm are shown in Figure 13. The simulations are in close agreement with the measured displacements throughout the course of shaking.

The deformed mesh with contours of maximum (engineering) shear strain for the end of shaking is shown in Figure 14. Note that FLAC reports the radius of the Mohr circle of strain, such that the values shown in this figure are twice those reported by FLAC. The computed deformation patterns and magnitudes are in reasonable agreement with those measured during testing. The simulation predicts that the soil-cement panels would develop engineering shear strains of up to about 8% near the base, even though the crack detectors showed cracking in only limited locations during this event.

The computed stress-strain response for a point in the loose Ottawa sand layer below the embankment crest (at the location of pore pressure transducer P1, Figure 3) is shown in Figure 15a. This figure shows the shear stress ratio on the horizontal plane (i.e. τ_{hv}/σ'_{vo}) versus the corresponding shear strain, γ_{hv}. The actual loading condition is more complex than pure simple shear, but this point is located in an area dominated by simple-shear deformations so examining the response along a horizontal plane is reasonable. The computed stress-strain response shows the loss of soil stiffness in the first couple of cycles as pore pressures rose rapidly, followed by a progressive accumulation of shear strains with each cycle of loading. The computed responses in this layer are consistent with the behaviors expected based on the single-element simulations performed during the constitutive model calibration process (e.g. Figures 8 and 9, and Ziotopoulou and Boulanger 2016).

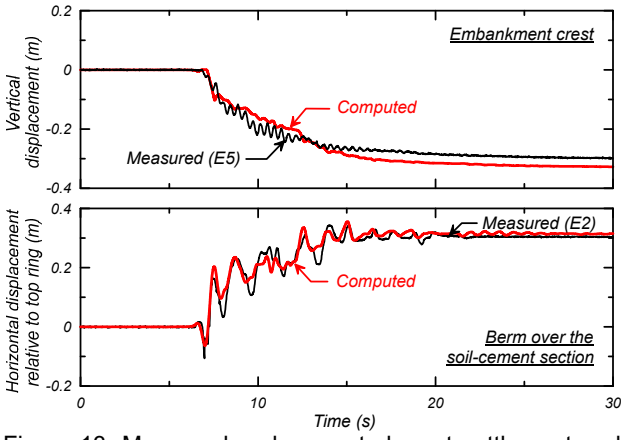

Figure 13. Measured and computed crest settlement and berm horizontal displacement for the Kobe 0.26 g event

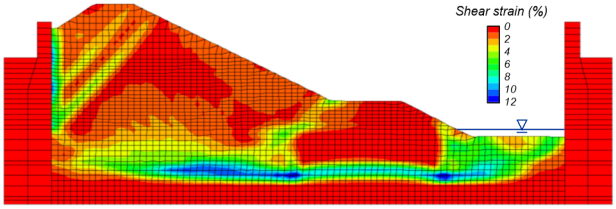

Figure 14. Contours of shear strain after shaking for the simulation of the Kobe 0.26 g event

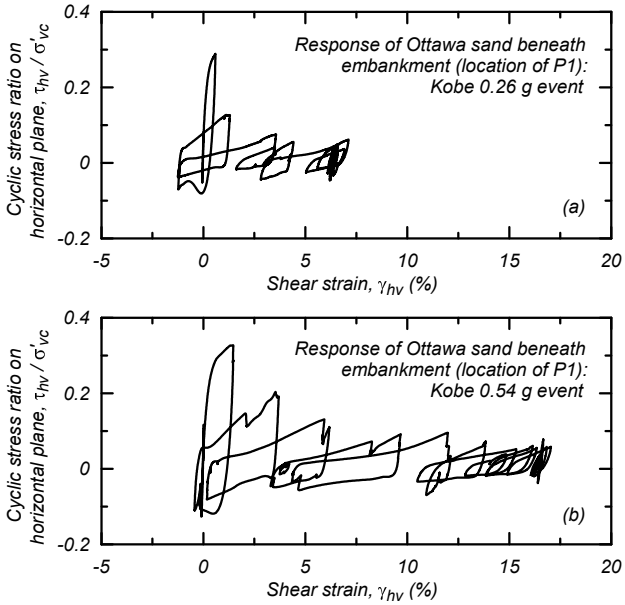

Figure 15. Stress-strain response for a point in the loose Ottawa layer beneath the embankment crest (location of P1) during: (a) Kobe 0.26 g and (b) Kobe 0.54 g events

5.2 Kobe event with PBA = 0.54 g

Simulated and measured accelerations for the PBA = 0.54 g event are compared in Figure 16 for several points in the embankment, toe berm, foundation layer, and base. The measured accelerations in the loose sand layer exhibit some high frequency spikes that are associated with the cyclic mobility behaviors; the computed responses capture this cyclic mobility response but underestimate the magnitude of the acceleration spikes. The simulations are otherwise in reasonable agreement with the recordings throughout the embankment and foundation.

Simulated and measured pore pressures for several points in the loose sand layer are compared in Figure 17. The simulations reasonably track the rise in excess pore pressures, their peak values, and their dissipation rates after the end of strong shaking.

Simulated and measured displacements for the crest and berm are shown in Figure 18. The computed horizontal displacement of the berm is in good agreement with the measured displacement throughout shaking, whereas the compute crest settlement is about 80% greater than the measured displacements.

The deformed mesh with contours of shear strain for the end of shaking with the PBA = 0.54 g event are shown in Figure 19. The simulation predicts that the soil-cement panels would develop engineering shear strains of up to about 30% near their base, which is consistent with the observation that they shear through during this event (Figure 5). The simulations also predict that the shear strains in the walls would be concentrated along their connection with the concrete base layer, whereas the post-testing photographs in Figure 5 show that the cracks start at about ¼ to ½ the wall height on the upslope end, are

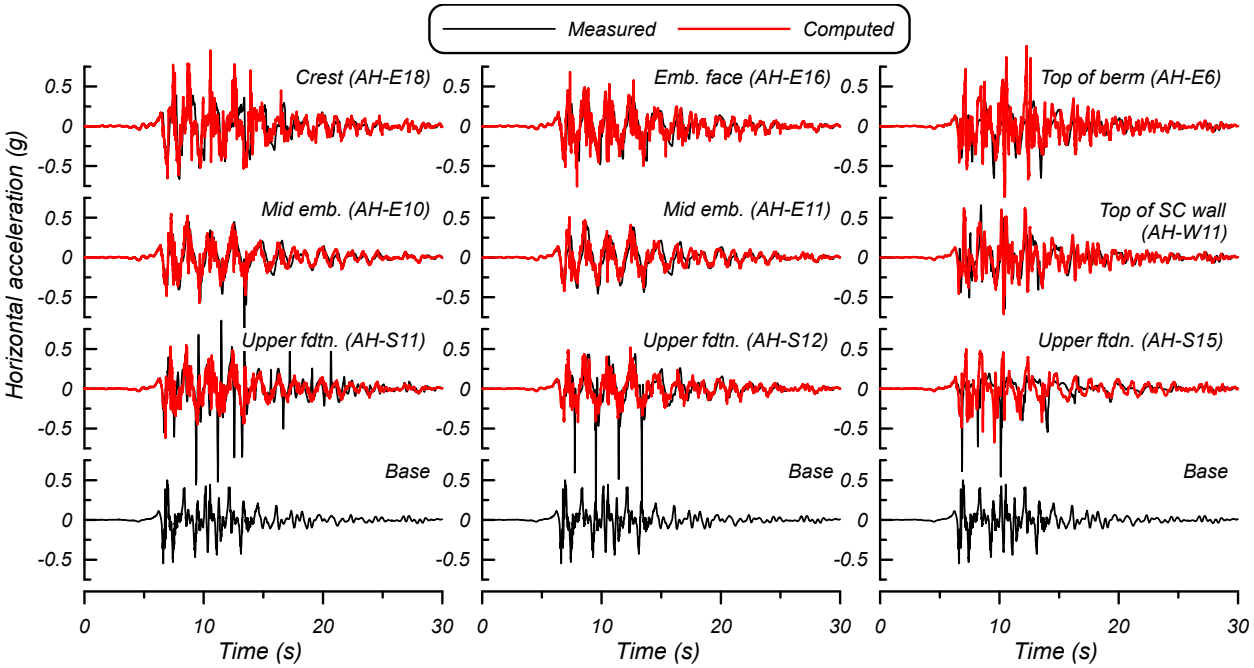

Figure 16. Measured and computed accelerations for the Kobe 0.54 g event

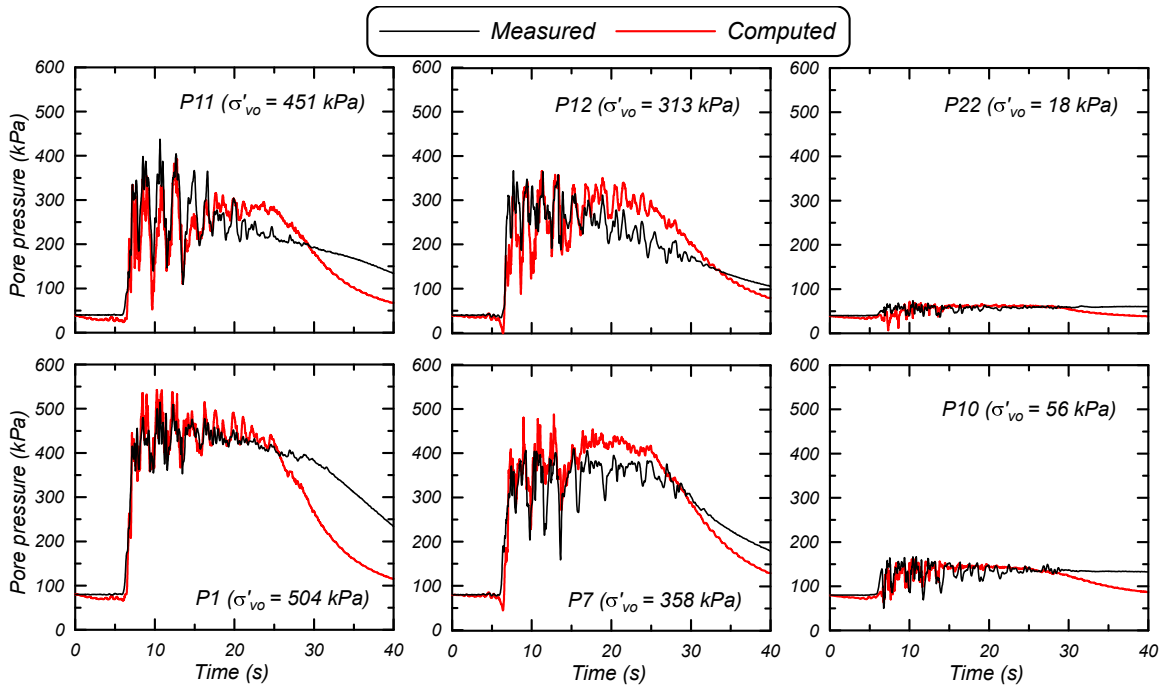

Figure 17. Measured and computed excess pore water pressures for the Kobe 0.54 g event

closer to the bottom of the walls at the downslope end, and had irregular wavy surfaces that varied between walls.

The simulation also shows a shear plane extending up through the dense Monterey sand berm just upstream of the soil-cement treatment zone, along with complementary shear planes dipping down to the left in the embankment against the left side of the container (Figure 19). These shear bands indicate a rotational mechanism of embankment deformation that would increase crest settlement without increasing horizontal berm displacements (at the location of the displacement measurements). This mechanism is also evident in the shear strain contours for the smaller PBA = 0.26 g event (Figure 14), although the strains were much smaller. This

mechanism of embankment deformation in the simulations appears more significant that observed in the experiments, which may be one factor contributing to over-prediction of crest settlements (Figure 13).

The computed stress-strain response at the location of pore pressure transducer P1 (Figure 3) is shown in Figure 15b. The computed stress-strain response again shows the loss of soil stiffness in the first couple of cycles as pore pressures rose rapidly, followed by a progressive accumulation of shear strains with each cycle of loading. The shear strains in this event accumulate a bit more than twice as rapidly as during the PBA = 0.26 g event (Figure 15a), which was expected given the stronger shaking intensity. For both events, the shear stress acting on the soil element at the end of shaking is smaller than at the start of shaking because shear stresses have been redistributed to the surrounding stiffer zones (i.e. the embankment and soil-cement wall zone). The computed responses and their differences in the two events are again consistent with the behaviors expected based on single-element simulations performed during the constitutive model calibration process (e.g. Figures 8 and 9, and Ziotopoulou and Boulanger 2016).

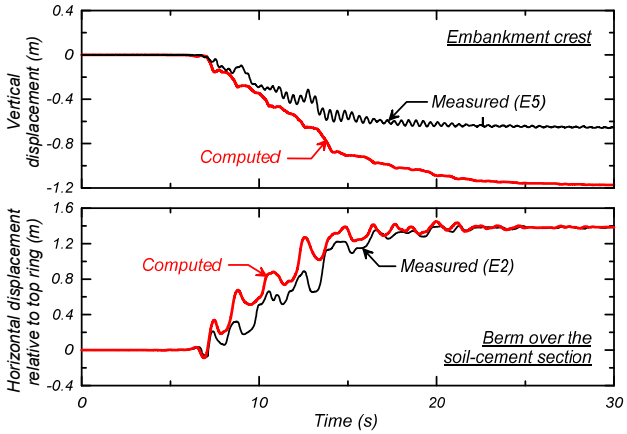

Figure 18. Measured and computed crest settlement and berm horizontal displacement for the Kobe 0.54 g event

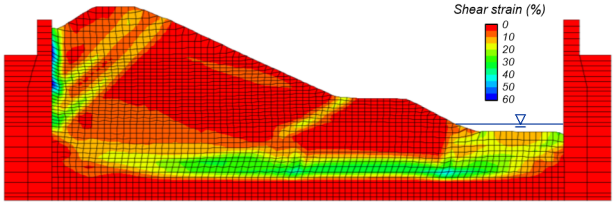

Figure 19. Contours of shear strain after shaking for the simulation of the Kobe 0.54 g event

5.3 Non-treated embankment

Simulations were repeated with the treatment zone omitted from the numerical model to provide a basis for evaluating the effectiveness of the soil-cement walls in reducing deformations. The deformed shape with contours of shear strain for the non-treated embankment subjected to the PBA = 0.54 g event is shown in Figure 20. The crest settled 3.1 m (about 4.7 times the measured value) and the berm displaced horizontally 5.0 m (about 3.6 times the measured value). These results illustrate that the soil-cement walls were effective in substantially reducing deformations relative to those that would be expected in the absence of the foundation improvement.

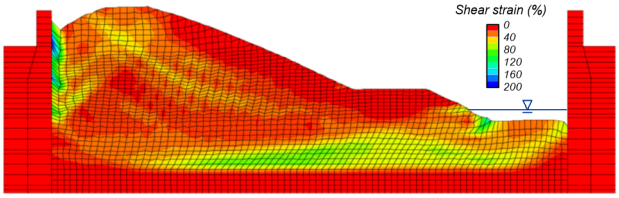

Figure 20. Contours of shear strain after shaking with the Kobe 0.54g event for the model without any soil-cement treatment zone (i.e. the non-treated case)

6 DISCUSSION

The numerical approximation of the treatment zone as a Mohr Coulomb material with equivalent composite properties does not account for a number of complex interaction mechanisms. Post-test excavation of the centrifuge model (Figure 6) showed that deformation of the treatment zone included a component of the enclosed liquefied sand displacing relative to the soil-cement walls (i.e. extruding between the walls). The significance of this extrusion mode to the overall deformations varied across the centrifuge container and appeared to vary along the length of the walls (e.g., local slumping of the overlying berm at the downstream toe would be expected to increase the role of extrusion near the downstream end of the walls). The post-test inspections of soil-cement walls showed irregular cracking and offsets that varied along the length of the walls and between adjacent walls (Figure 5). The development of offsets along these undulating crack surfaces was likely accompanied by local fluctuations in normal stress. Those changes in normal stress would contribute to changes in excess pore pressure, beyond those due to shearing alone. The net average excess pore pressures in the soil-cement during shearing would be expected to be negative based on typical undrained shearing responses of soil-cement specimens, the measured strength of the soil-cement for this model test, and the range of overburden stresses acting in this model test (e.g. Tatsuoka and Kobayashi 1983). Excess pore pressures in the enclosed liquefied sand would be expected to diffuse into the cracks in the soil-cement walls during strong shaking, which would be expected to reduce the mobilized shear resistance in the walls. The rate of pore pressure diffusion from the liquefied sand into these cracks would depend on the soil's hydraulic conductivity, the aperture of the wall cracks, the wall thickness, and the difference in pore pressures between the soil and wall materials. In addition, the shear resistance provided by the walls would be expected to degrade progressively during shaking as the cracks grow and develop offsets.

These mechanisms of potential strength loss in soil-cement wall systems during strong shaking are too complex to simulate directly in most practical applications, and hence it is common to use simpler equivalent composite system models with conservative selections for the input parameters/strengths. The good agreement obtained between 2D numerical simulations and measured centrifuge model responses in the present study suggest that equivalent composite system models may be a reasonable approximation for the type of embankment system examined in this centrifuge model study.

7 CONCLUSIONS

Two-dimensional nonlinear dynamic analyses were presented for a centrifuge model of an embankment dam on a liquefiable foundation layer treated with soil-cement walls. The centrifuge model corresponded to a 28 m tall embankment underlain by a 9 m thick saturated loose sand layer. Soil-cement walls were constructed through the loose sand layer over a 30 m long section near the toe of the embankment with a replacement ratio of 24%. The model was shaken with scaled earthquake motions having peak horizontal base accelerations of 0.05 g, 0.26 g, and 0.54 g. The numerical solutions were performed using the finite difference program FLAC (Itasca 2016) with the user-defined constitutive model PM4Sand (Boulanger and Ziotopoulou 2015) for the foundation and embankment sands. The soil-cement treatment zone was represented in the 2D analyses as a Mohr-Coulomb material with composite, area-weighted properties. The average shear strength of the soil-cement during shaking was taken as 80% of its peak undrained shear strength, which in turn was taken as one-half its unconfined compressive strength.

The results of the numerical simulations were in reasonable agreement with the recorded dynamic responses, including the triggering of liquefaction in the loose sand layer during the PBA = 0.26 g and 0.54 g events. The simulations reasonably approximated the observed deformation magnitudes and patterns, and correctly predicted that the soil-cement walls would shear through their full length in the largest shaking event. The results of these comparisons provide support for the use of these numerical modeling procedures, including the representation of a treatment zone with area-weighted composite properties, for analyses of embankment dams with soil-cement treatment of liquefiable soils in their foundations.

8 ACKNOWLEDGMENTS

The centrifuge tests were supported by the State of California though the Pacific Earthquake Engineering Research Center (PEER). The numerical simulations were supported in part by the California Department of Water Resources (DWR) under Contract 4600009751. Any opinions, findings, or recommendations expressed herein are those of the authors and should not be interpreted as representing the official policies, either expressed or implied, of either organization.

9 REFERENCES

Armstrong R. J. and Boulanger R. W. 2015. Numerical simulations of liquefaction effects on piled bridge abutments. 6th Intl Conf on Earthquake Geotechnical Engineering, Christchurch, New Zealand.

Barron R. F., Kramer C., Herlache W. A., Wright J., Fung H., and Liu C. 2006. Cement deep soil mixing remediation of Sunset North Basin Dam. Dam Safety 2006, ASDSO.

Bolton, M. D. (1986). The strength and dilatancy of sands. Géotechnique 36(1), 65–78.

Boulanger, R. W., and Ziotopoulou, K. 2013. Formulation of a sand plasticity plane-strain model for earthquake engineering applications. Journal of Soil Dynamics and Earthquake Engineering, Elsevier, 53, 254-267, dx.doi.org/10.1016/j.soildyn.2013.07.006.

Boulanger R.W. and Ziotopoulou K. 2015. PM4Sand (Version 3): A sand plasticity model for earthquake engineering applications. Report No. UCD/CGM-15/01, Center for Geotechnical Modeling, UC Davis, CA.

Friesen S. and Balakrishnan A. 2012. General approach used for the seismic remediation of Perris Dam. Proc. 32nd Annual USSD Conference, United States Society on Dams.

Fukutake K, Ohtsuki A. (1995). Three dimensional Liquefaction analysis of partially improved ground. Proc., First Intl Conf on Earthquake Geotechnical Engineering. Japan, 863-68.

Itasca 2016. FLAC, Fast Lagrangian Analysis of Continua, User's Guide, Version 8.0. Itasca Consulting Group, Inc., Minneapolis, MN.

Kirby R. C., Roussel G. L., Barneich J. A., Yiadom A. B. and Todaro S. M. 2010. Design and construction of seismic upgrades at San Pablo Dam using CDSM. 30th Annual USSD Conference, United States Society on Dams, pp. 137-151.

Khosravi, A., Khosravi, M., Yunlong, W., Pulido, A., Wilson, D. W., and Boulanger, R. W. 2016. Remediation of liquefaction effects for a dam using soil-cement walls: Data Report 1: Test AKH01. Report UCD/CGMDR-16/01, Center for Geotechnical Modeling, University of California, Davis, CA, October.

Khosravi, A., Khosravi, Boulanger, R. W., Wilson, D. W., and Pulido, A. 2017. Dynamic centrifuge test of an embankment on liquefiable soil reinforced with soil-cement walls. Proc., Performance-based Design in Earthquake Geotechnical Engineering, PBD-III, Vancouver, July 16-19.

Namikawa, T., Koseki, J., and Suzuki, Y. 2007. Finite element analysis of lattice-shaped ground improvement by cement-mixing for liquefaction mitigation. Soils and Foundations, 47(3), 559–76.

Parra Bastidas A.M., Boulanger R.W., DeJong J.T., and Price A.B. 2017. Effects of pre-strain history on the cyclic resistance of Ottawa sand. 16th World Conf on Earthquake Engineering, 16WCEE, paper 1213.

Tamura, S., Khosravi, M., Wilson, D. W., Rayamajhi, D., Boulanger, R. W., Olgun, C. G., and Wang, Y. 2017. Simple method for detecting cracks in soil-cement reinforcing elements for geotechnical centrifuge tests.

International Journal of Physical Modelling in Geotechnics, in review.
Wooten L. and Foreman B. 2005. Deep soil mixing for seismic remediation of the Clemson upper and lower diversion dams. 25th Annual USSD Conference, United States Society on Dams.
Zhang, F, and Fredlund, D. G. 2015. Examination of the estimation of relative permeability for unsaturated soils. Canadian Geotechnical Journal, 52: 2077-2087.
Ziotopoulou, K., and Boulanger, R. W. 2013. Calibration and implementation of a sand plasticity plane-strain model for earthquake engineering applications. Journal of Soil Dynamics and Earthquake Engineering, 53, 268-280, dx.doi.org/10.1016/j.soildyn.2013.07.009.
Ziotopoulou K. and Boulanger, R.W. 2016. Plasticity modeling of liquefaction effects under sloping ground and irregular cyclic loading conditions. Journal of Soil Dynamics and Earthquake Engineering; 84:269-283, 10.1016/j.soildyn.2016.02.013.